metals

MDPI

Article

Process Intensification for Rare Earth Elements Adsorption by Resonant Vibratory Mixing (RVM)

Mehran Saddat [1,*], Zainab Nasrullah [1], Frank Agyemang [1] and Richard LaDouceur [2]

[1] Department of Metallurgical and Materials Engineering, Montana Technological University, Butte, MT 59701, USA; znasrullah@mtech.edu (Z.N.); fagyemang@mtech.edu (F.A.)
[2] Department of Mechanical Engineering, Montana Technological University, Butte, MT 59701, USA; rladouceur@mtech.edu
* Correspondence: msaddat@mtech.edu

Abstract

Rare earth elements (REE) are critical to 21st-century technology, from electronics and defense applications to renewables and beyond. The processing of REE is primarily based on minerals (bastnasite, monazite, and xenotime), but alternative resources (coal ash, E-waste, and permanent magnets) are also gaining increasing interest. Adsorption remains one of the most efficient, environmentally friendly extraction methods despite its lengthy mixing time. In the present research article, a hemp biochar prepared by vacuum pyrolysis at 700 °C was examined for its applicability in the adsorption of selected REE (La^{3+}, Nd^{3+}, Dy^{3+}) from synthetic solutions. An innovative technique, Resonant Vibratory Mixing (RVM), was applied to improve adsorption kinetics, with factors including time (5–30 min) and intensity (30–70%) at room temperature. Using the Thermo Scientific 4000 M shaker for mixing, the maximum adsorption capacities were 77.56 mg/g for Dy^{3+}, 75.85 mg/g for La^{3+}, and 72.65 mg/g for Nd^{3+} using 100 mg of hemp biochar and 10 mL solutions (1000 mg/L). The adsorption capacity of 100 mg hemp biochar was 79.79 mg/g for Dy^{3+}, followed by 77.61 mg/g for La^{3+} and 75.75 mg/g for Nd^{3+}, using RVM for only 40 min at 70% intensity. RVM increased the adsorption capacities of all REE in only 40 min. Surface and structural analyses were carried out using Scanning Electron Microscope (SEM), Fourier Transform Infrared Spectroscopy (FTIR), Brunauer-Emmett-Teller analysis (BET), Zeta Potential, and Carbon/Hydrogen/Nitrogen (CHN) methods. The adsorption recoveries of all REE in the single-element system were higher than 98.5%. However, in a multi-element system, the adsorption recoveries of La^{3+}, Nd^{3+}, and Dy^{3+} were 83.7%, 96.2%, and 99.2%, respectively, demonstrating that hemp biochar has low selectivity for Dy^{3+} and Nd^{3+}. The adsorption process could be well described by the Langmuir isotherm and the pseudo-second-order kinetic model, indicating monolayer adsorption and chemical process involvement. Based on the characterization analysis of hemp biochar, electrostatic interaction was the dominant mechanism in this study. REE desorption using 0.5 M nitric acid was the most efficient, with >80% of REE recovered. The combination of hemp biochar as an adsorbent and RVM as a mixing technique demonstrated excellent performance in synthetic solutions; the reusability and application of hemp biochar to natural solutions require further study.

Keywords: biomass; pyrolysis; hemp biochar; rare earth elements (REE); sustainable REE adsorption; synthetic solutions; (resonant vibratory mixing) RVM

Check for updates

Academic Editor: Corby G. Anderson

Received: 23 July 2026
Revised: 16 August 2026
Accepted: 18 August 2026
Published: 1 September 2026

Copyright: © 2026 by the authors. Licensee MDPI, Basel, Switzerland. This article is an open access article distributed under the terms and conditions of the Creative Commons Attribution (CC BY) license.

1. Introduction

This work investigates the potential of hemp-derived biochar as a sustainable adsorbent for recovering La^{3+}, Nd^{3+}, and Dy^{3+} from synthetic solutions, using (Resonant Vibratory Mixing) RVM as an innovative mixing technique to enhance adsorption kinetics. This study hypothesized that adsorption is primarily determined by electrostatic interactions, based on the physicochemical properties of hemp-based biochar, which has a porous structure, a high surface area, and a negative surface charge. Moreover, RVM is predicted to allow adsorption times of minutes rather than hours and to enhance adsorptive capacity. This work strives to overcome the kinetic limitations of adsorption systems and offers a process-intensified approach for efficient REE recovery.

REE belong to a series of lanthanides that consist of 15 elements and yttrium (Y^{3+}) and scandium (Sc^{3+}) [1,2]. They play vital roles in most modern technologies such as electronics, renewable energy systems, and defense applications; therefore, global demand has been steadily rising [3–5]. However, the use of REE still faces technical challenges due to their close chemical similarity and the complexity of their occurrence in ores and secondary resources [6]. This has led to the need for more efficient, selective, and sustainable extraction methods.

Common hydrometallurgical techniques, including ion exchange, precipitation, chemical leaching, and solvent extraction, are used to process REE from various sources [7–10]. Adsorption has been considered a potential alternative due to its operational simplicity, cost-effectiveness, and lower environmental impact [4,5,10,11]. Despite these advantages, adsorption-based systems are limited by slow kinetics due to mass-transfer limitations and poor mixing. These constraints lead to lower process efficiency and significant operational time, which limit scalability. Therefore, there is a pressing need to improve the adsorption kinetics of REE on biochar surfaces using an optimized mixing technique.

RVM offers a potential solution to this problem by using low-frequency, high-amplitude vibrations to create a uniform micro-mixing zone within the vessel. Unlike other conventional mixing techniques, RVM ensures homogeneous mixing of components and improves material flow. It reduces mixing time compared to traditional mixers to achieve similar results [12]. RVM also eliminates the need for cleaning between batches and reduces contamination risk when properly operated [13]. RVM also accommodates reactors or containers of different sizes, enabling rapid mixing of various materials without cross-contamination [13]. Previous applications of RVM include the extraction of Sm-Co from magnets, which have been shown to positively affect Co uptake [14,15].

Biochar is a carbon-rich substance produced from various biomass sources. The carbonization process converts biomass into carbon-rich and stable materials. The usage of biochar is essential for minimizing agricultural waste and improving sustainability [16–19]. The biochar's elemental composition includes H_2, O_2, and higher levels of carbon (over 60%), which contribute to its highly porous structure, which is vital for adsorption [20,21]. To characterize biochar properties, analytical techniques such as SEM, FTIR, BET, X-ray Diffraction (XRD), Zeta Potential, Thermogravimetric Analysis (TGA), and Raman are used to determine surface morphology, surface functional groups, surface area and porosity, carbon crystallites in biochar, surface charge, gasification, and graphitization degree, respectively [22].

2. Materials and Method

2.1. Materials

Hemp biomass was collected locally in north central Montana, United States. Biomass was reduced in size through milling, but particle size was not controlled. Hemp biochar was produced in the absence of oxygen using a pyrolysis furnace via vacuum pyrolysis at 700 °C (10 °C/min) and held at this temperature for 75 min. Atmospheric pressure was set to 0.161 kPa. The furnace was then cooled to 25 °C, and the hemp biochar was removed

after 3 h of cooling. The hemp biochar was further removed and placed in a desiccator to prevent moisture absorption.

Solid REE chlorides (lanthanum (III) chloride hexahydrate, neodymium (III) chloride hexahydrate, and dysprosium (III) chloride hexahydrate) were obtained from STREM Chemical Inc. (Newburyport, MA, USA). All three solid REE chlorides had a purity of 99.9%. Three single-element synthetic solutions were prepared for La^{3+}, Nd^{3+}, and Dy^{3+}, and a mixed-element/multi-element solution was prepared from their chlorides. Synthetic solution concentrations ranged from 10 ppm to 1000 ppm. Figure 1 presents the process flow sheet for the research study, outlining steps from hemp biochar production to sample analysis via an Agilent 5800 (Santa Clara, CA, USA) Inductively Coupled Plasma Optical Emission Spectroscopy (ICP-OES) present in the Center for Advanced Materials Processing (CAMP) at Montana Technological University, Butte, MT, USA.

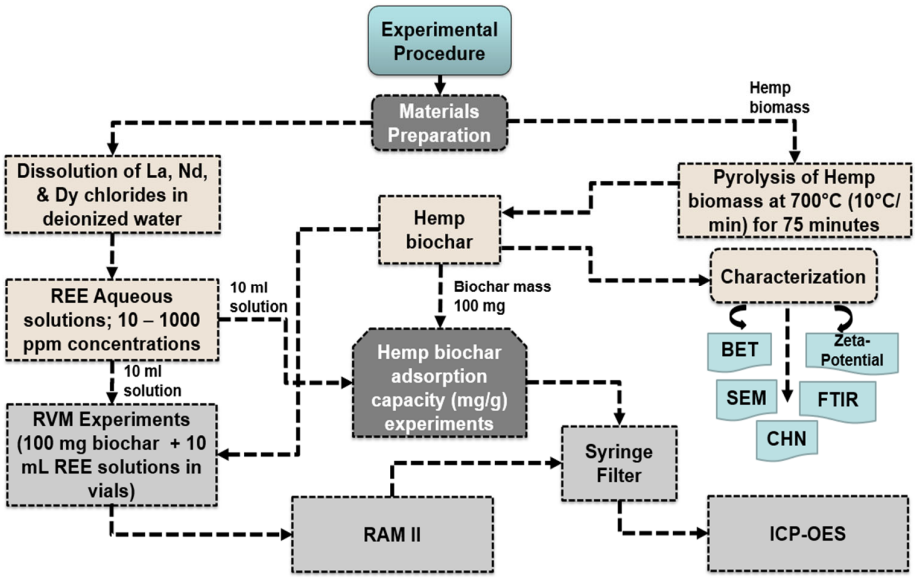

Figure 1. Process flowsheet for the process intensification of REE adsorption via RVM using hemp biochar.

2.2. Methods

2.2.1. REE Stock Solution Preparation

The solutions were prepared by dissolving the required amounts of these REE masses in 1000 mL of deionized (DI) water. The pH of the prepared solutions was determined using a METTLER TOLEDO SevenExcellenceTM pH meter in the Carbon-High Temperature Research (CHAR) Lab at Montana Technological University, Butte, Montana (MT), United States of America (USA). The solutions were stored in sealed bottles to avoid contamination.

2.2.2. Design of Experiments (DOE)

Analysis of variance (ANOVA) was used to assess variability in responses for the RVM operating parameters. The experimental design was created in Stat-Ease 360 Design-Expert software (Version 25). For the experiments, response surface methodology (RSM) was applied using a central composite design (CCD). Two RVM factors, time (5–30 min) and intensity (30–70%), were varied during adsorption and desorption experiments to explore REE recovery as the response variable. Table 1 shows the CCD experimental design. Midpoint experiments were replicated five times to determine reproducibility.

Table 1. Design of experiment for adsorption and desorption of La^{3+}, Nd^{3+}, and Dy^{3+} using RVM factors time (5–30 min) and intensity (30–70%), and response as La^{3+}, Nd^{3+}, and Dy^{3+} recovery.

Std	Run	Factor 1 A: Time Min	Factor 2 B: Intensity%	Response 1 La: Recovery wt%	Response 2 Nd: Recovery wt%	Response 3 Dy: Recovery wt%
6	1	32.4	50	-	-	-
4	2	30	70	-	-	-
7	3	17.5	26	-	-	-
12	4	17.5	50	-	-	-
13	5	17.5	50	-	-	-
1	6	5.0	30	-	-	-
10	7	17.5	50	-	-	-
3	8	5.0	70	-	-	-
2	9	30	30	-	-	-
5	10	2.6	50	-	-	-
9	11	17.5	50	-	-	-
11	12	17.5	50	-	-	-
8	13	17.5	74	-	-	-

2.2.3. Adsorption Capacity

The adsorption capacity experiments were performed using a Thermo-scientific 4000 M (Waltham, MA, USA) shaker (conventional mixing method) present in the CHAR Lab at Montana Technological University, Butte, MT, USA. For that, 10 mL of La^{3+}, Nd^{3+}, and Dy^{3+} solutions (1000 mg/L) and 100 mg hemp biochar were added to the 50 mL vials. The hemp biochar, solution pH (5), and solution volume were kept constant during the adsorption capacity experiments. The vials were placed horizontally on a Thermo-scientific 4000 M shaker. The adsorption capacity experiments were performed at room temperature (25 °C) and 350 rpm for 24 h. After the experiments, the solutions were filtered using 0.45 µm syringe filters. A 1 mL aliquot sample was taken from each filtered sample into a 15 mL centrifuge tube, and the samples were diluted with nitric acid (5%). The diluted samples were analyzed using ICP-OES.

To compare the RVM with the conventional mixing method, the adsorption capacity experiments were performed using the RVM. For that, 10 mL of La^{3+}, Nd^{3+}, and Dy^{3+} (1000 mg/L) and 100 mg hemp biochar were added to the 50 mL vials. The hemp biochar, solution pH (5), and solution volume were kept constant during the adsorption capacity experiments. The vials were placed in the RVM reactor. The adsorption capacity experiments were performed at 70% RVM intensity for 40 min. After the experiments, the solutions were filtered using 0.45 µm syringe filters. A 1 mL aliquot sample was taken from each filtered sample into a 15 mL centrifuge tube, and the samples were diluted with nitric acid (5%). The diluted samples were analyzed using ICP-OES.

2.2.4. RVM (Resonant Vibratory Mixing)

For this research project, RVM was used as a mixing technique to improve REE adsorption kinetics. As shown in Figure 2a, a reactor was designed and 3D printed from a resin (Formlabs Tough 2000, Somerville, MA, USA) to hold 20 mL scintillation vials. During the reactor design, it was also considered that the reactor fits easily into and out of the LabRAM II, as shown in Figure 2b.

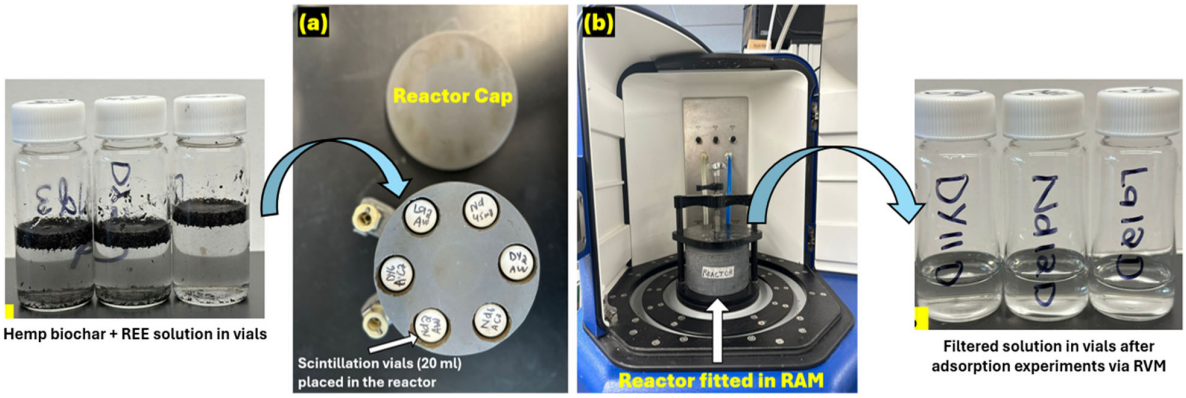

Figure 2. Image of the reactor along with the scintillation vials in it (**a**), image of the reactor fitted inside the Lab RAM II present in the CHAR Lab, Montana Technological University (**b**).

2.2.5. Adsorption Experiments Using RVM

For the adsorption experiments, the hemp biochar (100 mg) and 10 mL synthetic stock solutions (200 mg/L) of La^{3+}, Nd^{3+}, and Dy^{3+} were mixed in a 20-milliliter scintillation vial. The experiments were performed for single-element solutions (200 mg/L) to determine optimal operating characteristics and multi-element solutions (200 mg/L) to determine preference or selectivity for individual REE using hemp biochar. To improve adsorption kinetics, both sets of adsorption experiments were performed on the RVM at varying intensities (30–70%) and times (5–30 min). Afterward, the solutions were filtered using 0.45 µm syringe filters. Duplicate RVM adsorption experiments were performed to assess reproducibility and to prepare the biochar for desorption. In the first adsorption cycle, solutions were filtered with 0.45 µm syringe filters, while in the second cycle, cellulose filter paper (STERLITECH (Auburn, WA, USA) Cellulose Filter Paper, Grade CFP3) was used. After the adsorption experiments, one milliliter aliquot sample (1 mL) was taken from each filtered sample into a 15 mL centrifuge tube. The samples were diluted with 5% nitric acid and analyzed using an Agilent 5800 ICP-OES in the CAMP at Montana Technological University, Butte, MT, USA.

2.2.6. Characterization

The biochar's properties are essential to a better understanding of the adsorption process. Therefore, different characteristics of biochar were analyzed by various characterization techniques to evaluate the biochar's properties.

SEM present in the CAMP at Montana Technological University, Butte, MT, USA was used for the surface morphology of hemp biochar. The hemp biochar samples, before and after adsorption, were placed on a sample platform for SEM analysis. Before the SEM analysis, hemp biochar samples were carbon-coated using a Quorum Q150R Plus instrument present in the CAMP at Montana Technological University, Butte, MT, USA to improve electrical conductivity. SEM images were obtained using a MIRA3 TESCAN microscope at the CAMP, Montana Technological University, Butte, MT, USA.

The biochar sample was analyzed for functional groups using FTIR from Thermo-Scientific, Model No. Nicolet iS5 present in the Biology and Chemistry Department at Montana Technological University.

The adsorption–desorption isotherms of Nitrogen (N_2) were acquired using an Anton Paar Nova 800 present in CHAR Lab at Montana Technological at 77 K and used to determine the pore volume, pore width, and surface area of hemp biochar. Before analysis, the samples were vacuum degassed at 240 °C (10 °C/min, held for 240 min) to remove moisture and volatile contaminants. The surface area was determined using the BET

method based on adsorption data at relative pressures (P/P_o) ranging from 0.053 to 0.298. Pore volume and pore width were determined from desorption data using the DFT method.

Zeta-potential analysis was performed using an Anton Paar SurPASS 3.0 instrument present in Environmental Engineering Department at Montana Technological to determine the surface charge characteristics of hemp biochar. The hemp biochar sample was analyzed over a pH range of 2.0 to 11.0 to evaluate the pH-dependent surface charge characteristics and determine the point of zero charge (isoelectric point).

The LECO CHN 828 Analyzer present in CHAR Lab at Montana Technological was used to determine the carbon, hydrogen, and nitrogen content (%) in the hemp biochar sample. For the analysis, leak and system checks were performed first. Afterward, three blank samples were run, and 0.5 g of biochar sample was weighed, wrapped in aluminum foil, and rolled into a ball to fit into the sample holder. The ASTM D5373-21 and ASTM D5291-16 methods were used as standards for analysis [23].

2.2.7. Adsorption Kinetics and Isotherms

The adsorption experimental data obtained from adsorption capacity measurements and RVM were fitted to adsorption isotherms (Langmuir and Freundlich) and to kinetic models (pseudo-first-order and pseudo-second-order), respectively [24–26]. These models are essential for evaluating the adsorption mechanism, understanding the interaction between the adsorbent (hemp biochar) and the adsorbate (REE), and determining whether adsorption is monolayer or multi-layer [27]. The adsorption isotherms and kinetic models were compared and selected based on statistical fit (R^2), with realistic parameter values preferred [28,29].

2.2.8. Desorption Experiments

Desorption studies on REE-loaded hemp biochar from the second cycle of adsorption were conducted. The REE-loaded biochar was separated from the cellulose filter paper and dried in an oven at 50 °C for 24 h following adsorption. RVM grinding reduced the final biochar mass by about 5%, leaving approximately 95 mg in each experiment; this biochar mass was then placed in a 20 mL scintillation vial for desorption. Desorption experiments were conducted with 10 mL of 10% oxalic acid and 10 mL of 0.5 M nitric acid at room temperature as desorbing agents. The operating conditions were maintained consistent with those adopted in the adsorption experiments, where RVM intensities of 30–70% and contact times of 5–30 min were used. After desorption experiments, the solutions were filtered through filter paper (STERLITECH Cellulose Filter Paper, Grade CFP3). Each sample was analyzed using ICP-OES.

3. Results and Discussions

3.1. Characterization Results

3.1.1. SEM

Figure 3a shows the SEM image of hemp, indicating a fiber structure with no prominent porosity. The characteristics of parallel hemp fibers with smooth and vertically oriented surfaces are visible in Figure 3a. The hemp structure lacks visible, prominent pores due to the presence of volatiles. Therefore, pyrolysis is essential because it releases volatiles during thermal degradation [30]. These images were taken at 800× magnification.

Figure 3b shows an SEM image of hemp biochar before adsorption, clearly showing its porous structure after pyrolysis. The rough surface of biochar explains why REE adsorption occurred during both single-element and multi-element adsorption. Pores are readily observed in the SEM image, consistent with the BET analysis of pore volume and width.

The rough surface and porous structure of hemp biochar play an essential role in adsorption, as they capture REE ions.

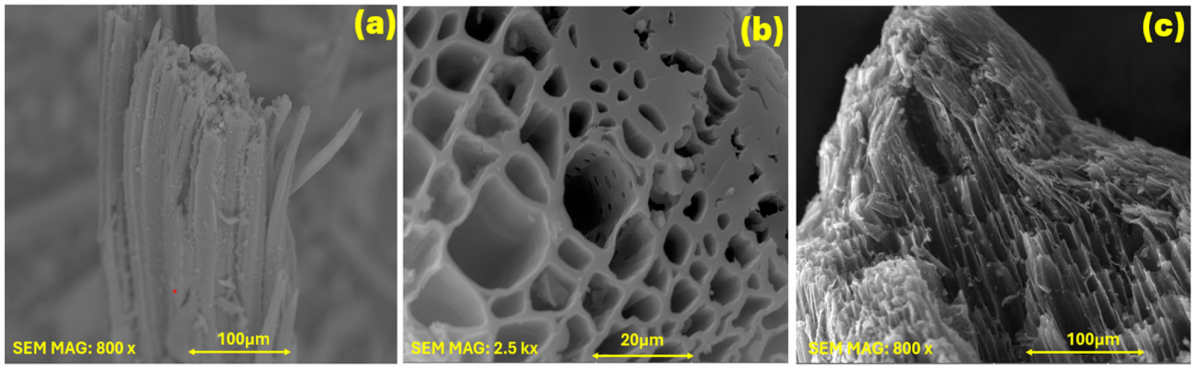

Figure 3. SEM images of hemp before the pyrolysis process (**a**), SEM images of hemp biochar taken before adsorption clearly show a porous structure (**b**), SEM images of hemp biochar after adsorption using RVM, showing a ruptured biochar surface (**c**).

Figure 3c illustrates an SEM image of hemp biochar after adsorption, where the porous structure has been ruptured and destroyed during the adsorption process. This structural disruption is probably due to a combination of factors. The repeated vibrational forces on the biochar pore walls are due to continuous agitation provided by the RVM, which can lead to weakening and fracturing of the thin biochar walls that separate adjacent pores. Both electrostatic attraction and ion exchange allow for localized charge accumulation and diffusive transport of REE ions into the pore network to weaken internal stress distribution across pore walls—another path toward bulk structural collapse. Capillary forces associated with solution uptake into the porous matrix during prolonged contact times (5–30 min) may cause swelling and subsequent wall breakage upon drying. Overall, these phenomena and chemical stresses account for the loss of the well-defined pore structure seen in Figure 3b. Therefore, adsorption recovery decreases in subsequent adsorption cycles as the biochar surface is destroyed during the first adsorption cycle [20]. This porous structure and its pores are also disturbed during desorption, especially with strong acids such as nitric acid, hydrochloric acid, and sulfuric acid [20]. Therefore, another reason for using oxalic acid in this research study was to achieve efficient desorption. It will address surface disturbance of hemp biochar, prevent its regeneration, and enable biochar to perform efficiently in subsequent adsorption–desorption cycles. This interpretation of structural disruption is based solely on qualitative SEM observations. No post-adsorption BET was performed in this study, so quantitative changes in surface area, pore volume, and pore width after adsorption could not be measured. Therefore, the hypothesized association between structural changes and improved adsorption efficiency is still associative rather than causal. Post-adsorption BET/DFT analysis: These solvation-based structural changes resulting from hydrogen bonding with the adsorbates will be introduced, and we identify post-adsorption BET/DFT analysis as a priority target for quantitative verification of these structures to adsorption performance in future work.

3.1.2. FTIR

Figure 4 illustrates the FTIR spectra of the hemp biochar. It was observed that the hemp biochar has no major functional groups. The peaks were consistent in four repeated analyses. The peaks were the same before and after adsorption, consistent with previous studies [31]. There were smaller peaks in the range of 1300 cm^{-1} to 1600 cm^{-1}. However, they could be unsaturated hydrocarbons, alkenes, and ethers [31]. The hemp biochar showed no carboxyl group, which is typically observed at higher wavenumbers. The smaller peaks observed

at wavenumbers above 3500 cm^{-1} could be alkenes and aromatics [26]. The spectrum was broadened from 680 cm^{-1} to 1320 cm^{-1}, then from 2400 cm^{-1} to 3500 cm^{-1}, which could be due to small CO_2 and moisture absorption from the atmosphere [32,33]. The minor peaks above 3500 cm^{-1} might be C-H stretching. Jaroslaw Molenda et al. concluded that the functional group of biochar depends strongly on pyrolysis temperature. Biochar produced at over 600 °C lacks functional groups in all biochar samples. The number of oxygen, carboxyl, and phenolic groups decreases at higher temperatures due to their degradation [34]. Banik C et al. also demonstrated that increased temperature reduces the number of oxygen heteroatoms from hydroxyl groups due to the predominance of condensed polycyclic aromatic structures [35,36]. Higher temperatures remove the functional groups and amorphous structure of biochar, whereas lower-temperature pyrolysis promotes the development of functional groups and carbon graphitization [34]. Since the hemp biochar was produced at 700 °C, it is primarily carbon. Therefore, it lacks major functional groups.

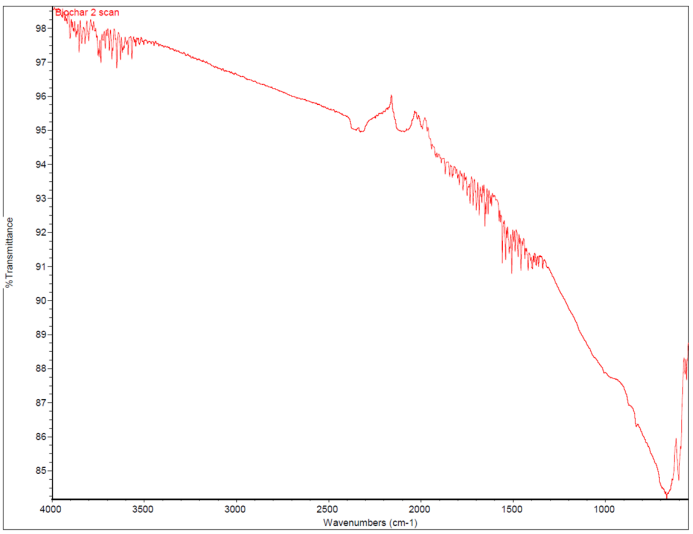

Figure 4. FTIR results of hemp biochar before adsorption.

3.1.3. BET

The hemp biochar surface textural properties, such as surface area, pore volume, and pore width, were determined using the BET and DFT methods based on N_2 adsorption–desorption. The average surface area, pore volume, and pore width of hemp biochar were 82.09 m^2/g, 0.0824 cm^3/g, and 2.655 nm, respectively. The surface area of hemp biochar is consistent with the pyrolysis temperature (700 °C). For accuracy and reliability, four samples were analyzed by BET. The standard deviation was 0.902, 0.0144, and 0.067 for surface area, pore volume, and pore diameter, respectively. Higher temperatures also tend to produce more carbon than lower temperatures. Islam et al. 2021 concluded that the surface area also increases with the carbon content increment [37].

The hemp biochar is categorized as a mesoporous material because it has an average pore diameter of 2.655 nm and exhibits hysteresis loops, indicating type IV isotherm curves. Thommes et al. and Wang et al. classified pores according to the S. Brunauer, L.S. Deming, W.E. Deming and E. Teller (BDDT) and International Union of Pure and Applied Chemistry (IUPAC) classifications, where mesopores are categorized as having diameters between 2 nm and 50 nm and exhibiting II and IV isotherm curves [38,39]. Wang et al. also reported that mesopores might increase with increasing temperature. Moreover, the increase in adsorbed amount with increasing relative pressure indicates the presence of mesopores

in the hemp biochar [40]. In this study, adsorption began at a lower relative pressure, indicating the presence of micropores on the hemp biochar surface (Figure 5a).

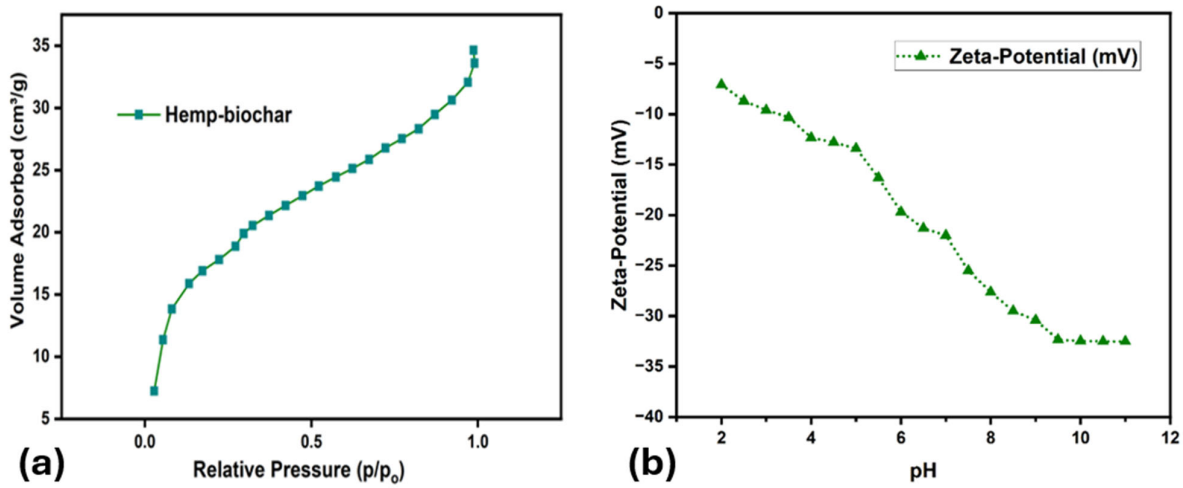

Figure 5. Volume adsorbed as a function of relative pressure for hemp biochar: as the relative pressure increases, the volume adsorbed also increases, indicating the presence of mesopores (**a**). Zeta potential of hemp biochar at various pH levels. Hemp biochar exhibits a negative zeta potential that increases with pH. The maximum zeta potential was observed at pH 9.5; it remained constant thereafter (**b**).

3.1.4. Zeta Potential

The zeta potential of hemp biochar decreased with increasing pH, due to deprotonation, making the biochar surface more negatively charged. Therefore, hemp biochar carries a negative surface charge with increasing pH. The zeta-potential values of hemp biochar ranged from −7.23 mV to −32.37 mV, indicating a more negative surface charge on hemp biochar, which favors REE adsorption via electrostatic attraction. Conversely, at low pH, functional groups protonate, giving a more positive surface charge. The zeta potential of hemp biochar as a function of pH is shown in Figure 5b. The point of zero charge (isoelectric point) was not determined, as the zeta-potential values remained negative across the entire pH range. This means that if the isoelectric point exists, it would be below pH 2.0. The zeta potential for hemp biochar was measured in the pH range of 2 to 11. However, the maximum zeta potential was observed in the pH range of 9.5 to 11. However, the boundary line for REE adsorption is at pH 6, since above pH 6, the REE start to precipitate as hydroxides [40]. At the same time, at lower pH, the electrostatic attraction between REE ions and the active site decreases due to the higher H^+ ions [40,41]. Therefore, the optimal pH for REE adsorption lies between 5 and 6.

3.1.5. CHN

The elemental composition of hemp biochar obtained from the CHN828 analysis indicates that hemp biochar contained carbon (66.3%), followed by hydrogen (1.26%), and nitrogen (0.844%). The carbon content is primarily dependent on the pyrolysis temperature. The literature reports that carbon content increases with increasing temperature [37]. Surface area is a function of carbon content, meaning that an increase in the surface area corresponds to an increase in carbon content [37]. The CHN results are consistent with the BET results, which determined the hemp biochar's average surface area. The hemp biochar also contained a small amount of N_2 and H_2. In addition to these elements, biochar may contain potassium, sodium, chlorides [42], and ash [43]. For hemp biochar produced under the stated conditions, the hydrogen-to-carbon ratio (H/C) was 0.23, which indicated a high

degree of carbonization. The low H/C ratio (0.23) also showed a more aromatic, stable carbon structure with lower volatile content.

3.2. Adsorption Capacity Results

The adsorption capacity of hemp biochar was 77.56 mg/g for Dy^{3+}, followed by 75.85 mg/g for La^{3+} and 72.65 mg/g for Nd^{3+}, using a Thermo-scientific 4000 M shaker for 24 h. On the other hand, the adsorption capacity of the same hemp biochar was 79.79 mg/g for Dy^{3+}, followed by 77.61 mg/g for La^{3+} and 75.75 mg/g for Nd^{3+}, using RVM for only 40 min at 70% intensity. The RVM increased the adsorption capacity of all REE by a small fraction of the time, as shown in Figure 6b. The adsorption capacity experiments were performed using 100 mg of hemp biochar, as the adsorption capacity is higher at lower biochar masses, as reported in the literature [11]. The active sites increase with increasing biochar mass, ultimately increasing REE uptake%. However, higher biochar mass reduces adsorption capacity because REE ions are distributed across more active sites [11]. The optimal solution pH was five. The solution's pH was selected based on previous studies in the literature [40,41,44]. For the hemp biochar adsorption capacity, the initial solution concentrations were changed from 10 mg/L to 1000 mg/L. It was determined that optimal concentrations were around 800 mg/L, indicating higher adsorption capacities for all REE in both cases. As seen in Figure 6a,b, the adsorption capacity increased with increasing initial concentration until the hemp biochar was saturated at around 800 mg/L for all REE, indicating a plateau. After that, the adsorption capacity remained relatively constant, indicating that the hemp biochar reached its practical adsorption capacity under the given experimental conditions (100 mg hemp biochar dose, pH 5, room temperature and initial REE concentration of 1000 mg/L) for both Thermo-scientific 4000 M shaker and RVM. The adsorption capacity was calculated using Equation (1), where C_0 (mg/L) denotes the initial concentration, C_e (mg/L) is the concentration at equilibrium, V (mL) is the volume of the adsorbate, and w (mg) is the adsorbent mass (biochar mass) [31].

$$Adsorption\ Capacity\ (\mathrm{mg/g}) = \frac{(C_0 - C_e)\ V}{w} \quad (1)$$

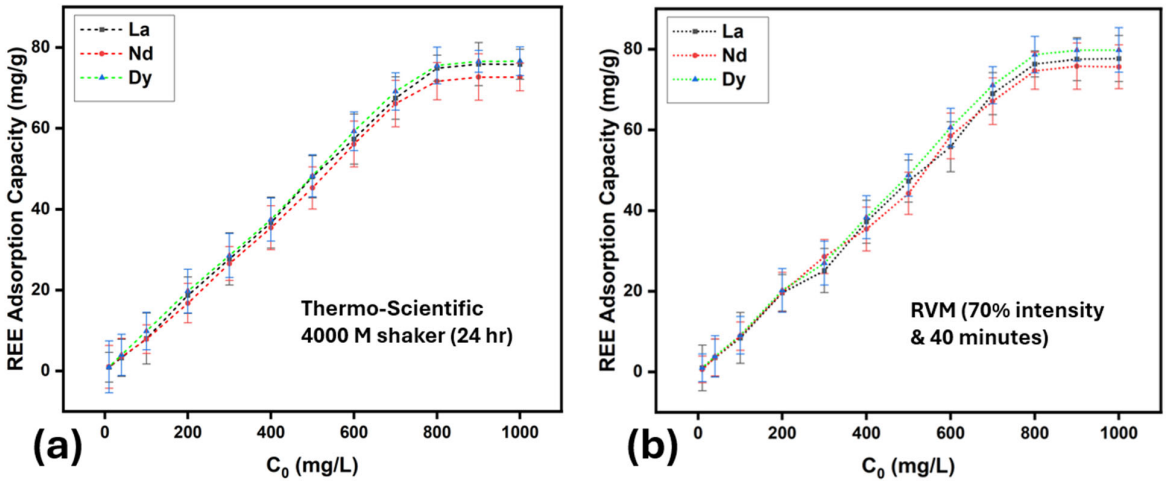

Figure 6. Adsorption capacity of 100 mg hemp biochar as a function of initial concentration at pH 5 using Thermo-scientific 4000 M shaker for 24 h (350 rpm) at room temperature (**a**), REE recovery as a function of initial concentration at pH 5 and 100 mg of hemp biochar using RVM for 40 min at 70% intensity (**b**).

3.3. REE Adsorption Results

3.3.1. RVM Single-Element Adsorption

Figure 7a shows the interaction plot of La^{3+} recovery as a function of RVM time and intensity in the single-element adsorption process. The time variable at lower intensity showed a negative correlation with La^{3+} recovery. At lower intensity (30%), as time increased, the recovery of La^{3+} adsorption decreased. In contrast, high intensity (70%) showed a positive correlation with La^{3+} recovery: as intensity increased, La^{3+} recovery also increased. The maximum adsorption recovery was 98.7% at 30 min and 70% intensity. The La^{3+} recovery was 92.6% at 30% intensity and 5 min, indicating that La^{3+} adsorption was faster in the first minutes due to the abundant active sites on the hemp biochar surface. In the literature, it is reported that more adsorbents improve active-site accessibility and increase the REE uptake% [11]. Additional data for all single-element adsorption experiments are provided in the Supplementary Materials.

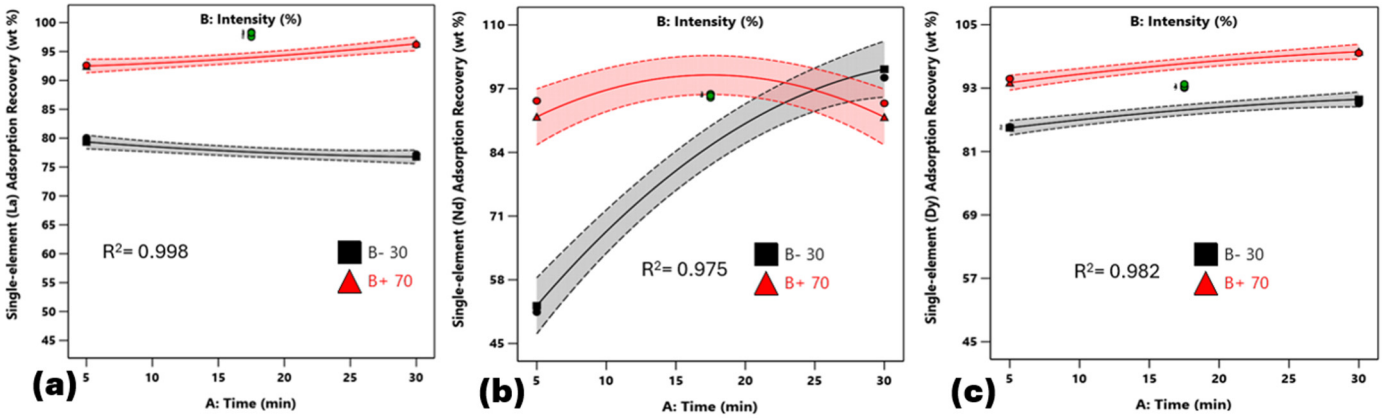

Figure 7. The interaction plots of REE recovery (%) as a function of time (5–30 min) and intensity (30–70%). Model-predicted responses with higher confidence intervals (shaded regions). Effect of RVM factors, time, and intensity on REE adsorption onto the biochar surface in a single-element adsorption process. (**a**) La^{3+}; (**b**) Nd^{3+}; (**c**) Dy^{3+}.

Figure 7b shows the interaction plot of Nd^{3+} recovery in the single-element adsorption process. Nd^{3+} recovery was positively affected by 70% intensity and 5–17.5 min; recovery increased. After that, the Nd^{3+} recovery decreased to 70% at higher intensity because electrostatic bonds between REE ions and the active sites could have been broken, allowing Nd^{3+} ions to be desorbed back into solution rather than adsorbed onto the hemp biochar surface. The Nd^{3+} recovery increased from 51.4% to 99.2% over 5–30 min at 30% intensity. The maximum Nd^{3+} recovery was 99.2%, observed at 30 min and 30% intensity, which is not the expected or preferential behavior. To further study and understand this unexpected behavior in Nd^{3+} adsorption, autosorb experiments are needed.

Figure 7c shows the interaction plot of Dy^{3+} recovery, which showed a positive correlation with both time and intensity. The Dy^{3+} recovery increased from 85.6% to 90.0% over 5–30 min at a lower intensity (30%). Similarly, at a higher intensity (70%), Dy^{3+} recovery increased from 94.7% to 99.6% over 5–30 min. Among the three REE, Dy^{3+} showed the highest adsorption on the surface of hemp biochar. Even at lower time and intensity, the Dy^{3+} recovery was 85.6%; this high recovery at lower time indicated that adsorption was rapid at the beginning and slowly increased with increasing time and intensity.

The above findings describe how RVM and its factors (time and intensity) can be strategically optimized for REE recovery on the hemp biochar surface. The models indicate that increasing intensity favors REE adsorption. However, time extension sometimes compensates for lower recovery at higher intensity, especially for Nd^{3+}. Adsorption affinity

increases with atomic number for heavy REE relative to light REE. It is also reported that smaller ionic radii lead to stronger adsorption, favoring the adsorption of heavy REE over light REE [11]. The smaller ionic radii of Dy^{3+} result in a higher charge density, as the charges are concentrated in a smaller volume, leading to stronger ionic interactions and coordination bonds. Adsorption was primarily affected by RVM intensity because, at higher intensity, collision frequency between REE ions and active sites increases, ion mass transfer is enhanced, and boundary-layer resistance is reduced. Therefore, in the single-element adsorption process, a higher time (up to 30 min) and intensity (up to 70%) lead to an increased recovery of REE adsorption, except for Nd^{3+}, whose recovery peaked at 30 min and 30% intensity.

The BET analysis of hemp biochar before adsorption also indicated high REE adsorption. The surface area, pore volume, and pore width of biochar provided accessible active sites for REE ions, enhancing favorable adsorption without functional groups on the hemp biochar surface. In addition, the SEM images confirmed the porous structure of the hemp biochar. This porous structure has active sites that function as capture or adsorption sites for REE. The negative surface charge of hemp biochar was another driving factor for REE adsorption, as REE are positively charged. The adsorption could be high due to electrostatic attraction between the negative charges on hemp biochar and the positive charges on REE ions [4].

3.3.2. RVM Multi-Element Adsorption

Figure 8a shows the La^{3+} recovery from a multi-element solution interaction plot using RVM. It was indicated that La^{3+} recovery showed a minimum negative correlation with time at lower intensity (30%), whereas it showed a stronger positive correlation with higher time and intensity (70%). The La^{3+} recovery showed a minimum time and a high-intensity dependency. La^{3+} recovery increased sharply from 55.8% to 83.7% with increasing time at higher intensity (70%). The maximum La^{3+} recovery from a mixed solution was 83.7%. La^{3+} recovery at lower intensity (30%) and time (5 min) was higher, suggesting abundant active sites. In contrast, it decreased as time was extended, since the lower intensity could not overcome the boundary-layer resistance. Therefore, the La^{3+} recovery was reduced at lower intensity. Additional data for all multi-element adsorption experiments are provided in the Supplementary Materials.

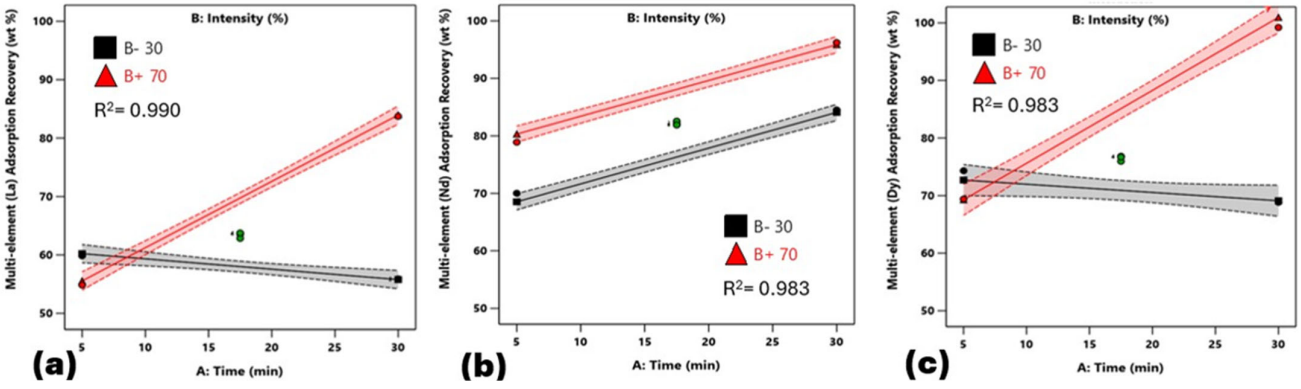

Figure 8. The interaction plots of REE recovery (%) as a function of time (5–30 min) and intensity (30–70%). Model-predicted responses with higher confidence intervals (shaded regions). Effect of RVM factors, time, and intensity on REE adsorption onto the biochar surface in a multi-element adsorption process. (**a**) La^{3+}; (**b**) Nd^{3+}; (**c**) Dy^{3+}.

Figure 8b illustrates the Nd^{3+} recovery interaction plot, which showed a strong dependence on both time and intensity, indicating a positive correlation with both in multi-element adsorption. The Nd^{3+} recovery increased from 70.0% to 84.5% as the time increased

from 5 min to 30 min at 30% intensity. Similarly, Nd^{3+} recovery rose from 78.9% to 96.2% as time increased at 70% intensity. The highest Nd^{3+} recovery was 96.2, achieved at a longer time (30 min) and a higher intensity (70%).

Figure 8c illustrates the Dy^{3+} recovery interaction plot. Dy^{3+} adsorption showed a positive correlation with 70% intensity and time, while a negative correlation with 30% intensity and time. The Dy^{3+} recovery increased from 69.7% to 99.1% as the time (5–30 min) was increased at 70% intensity. However, the Dy^{3+} recovery decreased from 71.3% to 68.2% as time increased from 5 to 30 min at 30% intensity, indicating a slight negative correlation. This data showed that the new technology's (RVM) parameters (time and intensity) can differ across REE solutions.

The surface properties of hemp biochar provided accessible active sites for REE ions, enhancing maximum adsorption. Moreover, the surface morphology, pore structure, and negative surface charge of the hemp biochar also contributed to REE adsorption in multi-element adsorption [4]. It was noted that the hemp biochar was slightly more selective for Nd^{3+} and Dy^{3+} REE than for La^{3+}. This low selectivity could be due to the smaller ionic radii and high charge density. For high REE selectivity, biochar needs to be modified or functionalized, thereby enabling more selective adsorption [11]. It was also observed that high intensity generally favors the adsorption of La^{3+}, Nd^{3+}, and Dy^{3+} in multi-element REE adsorption.

In contrast, extended time at lower intensity negatively affected the adsorption in multi-element REE adsorption, except for Nd^{3+}. High intensity promotes faster mass transfer, reduces boundary-layer resistance, and facilitates the transport of ions to the hemp biochar surface. Moreover, at high intensity, more surface collisions are likely to occur, and equilibrium is reached more quickly. These factors contributed to the favorable adsorption at high intensity using RVM. Once the sites are filled with ions and equilibrium is reached due to high intensity, extending the time makes little contribution to REE adsorption. Furthermore, the hemp biochar selectivity might be affected due to the same oxidation state of the REE; La^{3+}, Nd^{3+}, and Dy^{3+} have the same oxidation state (Trivalent). It is reported that adsorption favors higher oxidation states over lower ones because high-valence ions are more strongly attracted to the active sites [11].

3.4. Adsorption Kinetics and Isotherm Models

Figure 9a,b illustrates adsorption experimental data, which were fit to linearized forms of the pseudo-first-order and pseudo-second-order models to determine the REE adsorption mechanism on the hemp biochar surface. The pseudo-first-order model yielded R^2 values of 0.8354, 0.8341, and 0.8757 for La^{3+}, Nd^{3+}, and Dy^{3+}, respectively. The rate constants (k_1) for the model were 0.0527 min^{-1}, 0.0971 min^{-1}, 0.0783 min^{-1} for La^{3+}, Nd^{3+}, and Dy^{3+}, respectively, indicating that Nd^{3+} showed the fastest adsorption among REE. However, the $q_{e\ calc}$ was much lower than the $q_{e\ exp}$, indicating that the pseudo-first-order model inadequately described the adsorption behavior. More details are provided in Table 2.

Table 2. Pseudo-first-order kinetic model and pseudo-second-order kinetic model results for the adsorption of La^{3+}, Nd^{3+}, and Dy^{3+}.

Pseudo-First-Order Kinetic Model					**Pseudo-Second-Order Kinetic Model**				
	Units	**La^{3+}**	**Nd^{3+}**	**Dy^{3+}**		**Units**	**La^{3+}**	**Nd^{3+}**	**Dy^{3+}**
R^2	-	0.8354	0.8341	0.8757	R^2	-	0.9984	0.9917	0.9991
K_1	(min^{-1})	0.0527	0.0971	0.0783	K_2	(g/mg.min)	0.0722	0.0443	0.0887
qe_{Cal}	(mg/g)	2.6460	6.5920	2.7490	qe_{Cal}	(mg/g)	17.890	18.380	20.280
qe_{exp}	(mg/g)	17.780	18.191	20.136	qe_{exp}	(mg/g)	17.780	18.190	20.140
-	-	-	-	-	h	(mg/g.min)	23.112	14.970	36.500

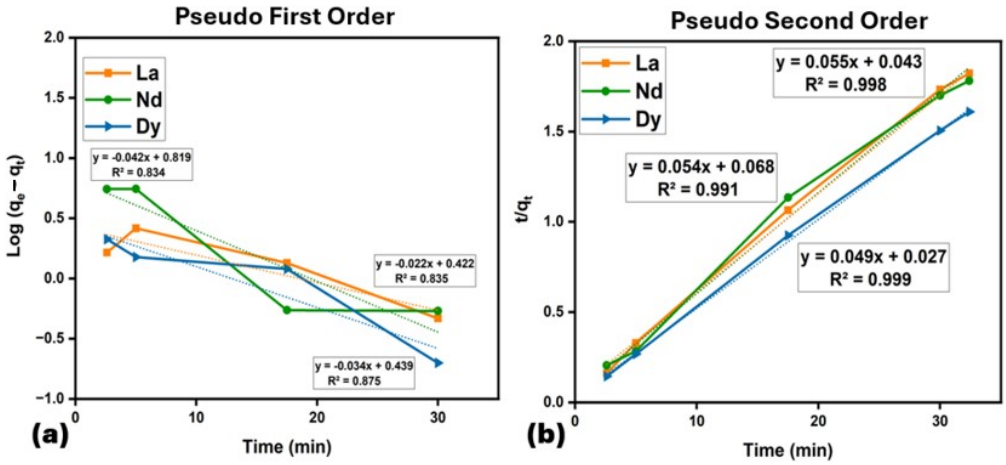

Figure 9. RVM experimental data fitted into pseudo-first-order kinetic model data (**a**), and pseudo-second-order kinetic model data (**b**), for the adsorption of La^{3+}, Nd^{3+}, Dy^{3+}.

The pseudo-second-order model yielded R^2 values of 0.9984, 0.9917, and 0.9991 for La^{3+}, Nd^{3+}, and Dy^{3+}, respectively. The rate constants (k_2) for the pseudo-second-order model were 0.0722 min^{-1}, 0.0443 min^{-1}, and 0.0887 min^{-1} for La^{3+}, Nd^{3+}, and Dy^{3+}, respectively, indicating a more superior fit than the pseudo-first-order model. The rate constant of Dy^{3+} showed the fastest adsorption kinetics. Moreover, the $q_{e\ calc}$ was almost identical to $q_{e\ exp}$, indicating remarkable agreement with the experimental data. The initial adsorption of Dy^{3+} ($h = k_2\ q_{calc}{}^2$) indicated that Dy^{3+} adsorbed rapidly onto the hemp biochar; this affinity may be due to Dy^{3+}'s smaller ionic radius and high charge density. Since the pseudo-second-order model fitted the adsorption experimental data using RVM, this suggested that a chemical process was involved, which was not the expected result. However, in this study, RVM was used as a mixing method; this may have contributed to the results. Therefore, a new model is suggested to fit the RVM adsorption experimental data and check the response. More details are provided in Table 2.

Figure 10 illustrates the adsorption capacity experimental data for all REE, which were fitted to the Langmuir and the Freundlich adsorption isotherm models. As shown in Figure 10a–c, the experimental data fitted the Langmuir model better than the Freundlich model, indicating monolayer adsorption. Moreover, the equilibrium stated that there was a limited number of active sites with identical energy; thus, saturation was achieved. Table 3. shows that the experimental data exhibited R^2 values of 0.997, 0.999, and 0.998 for La^{3+}, Nd^{3+}, and Dy^{3+}, respectively, indicating an excellent fit to the model. The q_{max} results demonstrate that hemp biochar has significant adsorption capacity for all three REE. Dy^{3+} has higher q_{max} values than La^{3+} and Nd^{3+}, indicating greater affinity for hemp biochar. Therefore, some selectivity for Dy^{3+} was observed, consistent with the multi-element adsorption shown in Figure 10. The hemp biochar adsorption capacity experimental data for all three REE were compared with the maximum monolayer adsorption capacity data from the Langmuir isotherm model. It showed a relative error of less than 2.5%, indicating that the adsorption capacity data fit the Langmuir model well. The relative errors were 2.25% for La^{3+}, 1.25% for Dy^{3+}, and 0.33% for Nd^{3+}. Langmuir and Freundlich model parameters were obtained by the non-linear regression (Microsoft Excel) method, minimizing the sum of squares residual between the experimental and predicted adsorption capacities using the Solver add-in. The linear and non-linear forms of the Langmuir and the Freundlich isotherm models are shown in Equations (2)–(5) in Table 4 [31,45]. However, for this study, the non-linear forms of the Langmuir and Freundlich Equations (2) and (3) were used for fitting, as shown in Table 4.

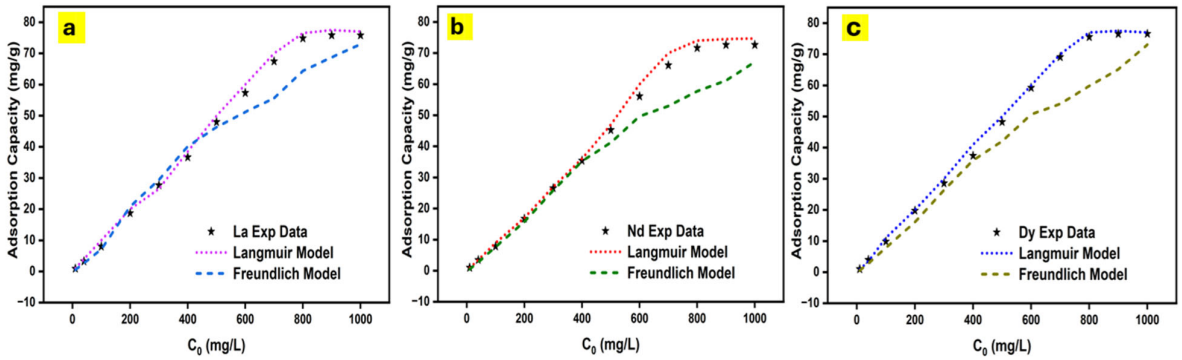

Figure 10. (**a**–**c**) Langmuir and Freundlich adsorption isotherm models were fitted to experimental data on the adsorption capacities of La^{3+}, Nd^{3+}, and Dy^{3+} using a Thermo Scientific 4000 M Shaker for mixing. The data from the hemp biochar adsorption capacity experiments are shown as stars in these graphs. Langmuir fit the experimental data better than the Freundlich model, indicating a monolayer adsorption process with active sites of identical energy.

Table 3. Langmuir and Freundlich adsorption isotherm models were used to predict adsorption capacities from experimental data for La^{3+}, Nd^{3+}, and Dy^{3+} using the Thermo Scientific 4000 M Shaker.

	Langmuir			**Langmuir q_{max} vs. Experimental Data**			**Freundlich**		
REE	**q_{max} (mg/g)**	**b (L/mg)**	**R^2**	**q_{max} (mg/g)**	**Adsorption Capacity (mg/g)**	**Error%**	**K_F (mg/g) (L/mg)$^{1/n}$)**	**n**	**R^2**
La^{3+}	77.56	0.325	0.997	77.56	75.85	2.25	71.23	5.74	0.912
Nd^{3+}	72.41	0.341	0.999	72.41	72.65	0.33	69.37	4.93	0.905
Dy^{3+}	78.53	0.665	0.998	78.53	77.56	1.25	74.11	6.62	0.918

Table 4. Linear and non-linear forms of Langmuir and Freundlich isotherm models.

Isotherm Model	**Non-Linear**	**Linear**	**Reference**
Langmuir	$q_e \frac{q_{max}\, b\, C_e}{1+b\, C_e}$ (2)	$q_e = K_F C_e^{1/n}$ (3)	[31,45]
Freundlich	$\frac{C_e}{q_e} = \frac{1}{q_{max} * b} + \frac{C_e}{q_{max}}$ (4)	$log_{qe} = log_{KF} + \frac{1}{n} log_{Ce}$ (5)	[31,45]

Where C_e is the concentration at equilibrium (mg/L), q_e is the adsorption capacity at equilibrium (mg/g), n is the adsorption intensity, q_{max} is the maximum monolayer adsorption capacity (mg/g), b is the Langmuir constant related to binding energy/affinity (L/mg), and K_F is the Freundlich constant indicating adsorption capacity (mg/g) (L/mg)$^{1/n}$).

3.5. Desorption Results

3.5.1. RVM Single-Element Desorption

Figure 11a shows the interaction plot of La^{3+} desorption in a single-element desorption process using 0.5 M nitric acid. The maximum desorption recovery was observed at higher time and intensity using RVM. The desorption recovery showed a positive correlation with intensity; La^{3+} desorption increased from 61% to 82.5% as time was increased using higher intensity (70%). The maximum La^{3+} desorption was 82.5%. The La^{3+} desorption recovery was lowest at a shorter time (5 min) and lower intensity (30%), consistent with the boundary-layer resistance concept. Additional data for all single-element desorption experiments are provided in the Supplementary Materials.

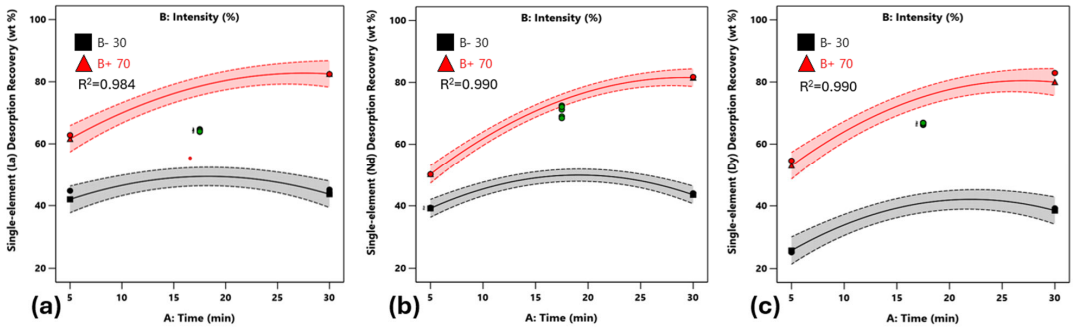

Figure 11. Interaction plots of REE desorption recovery (%) as a function of time (5–30 min) and intensity (30–70%). Model-predicted responses with high confidence intervals (shaded regions). Effect of RVM factors, time, and intensity on REE desorption into the solution from the biochar surface in a single-element desorption process using 0.5 M nitric acid. (**a**) La^{3+}; (**b**) Nd^{3+}; (**c**) Dy^{3+}.

Figure 11b illustrates the interaction plot of Nd^{3+} desorption recovery in a single-element desorption process using 0.5 M nitric acid. The maximum Nd^{3+} desorption recovery was 81.8% at higher time and intensity using RVM. The Nd^{3+} desorption recovery shows a positive correlation with higher intensity; Nd^{3+} desorption increased from 50% to 81.8% as time increased, with a higher intensity (70%). However, at lower intensity, the Nd^{3+} desorption recovery remained almost unchanged, with only a slight increase and then a decrease as time was extended.

Figure 11c illustrates the interaction plot of Dy^{3+} desorption recovery in a single-element desorption process using 0.5 M nitric acid. Similar to La^{3+} and Nd^{3+}, the maximum Dy^{3+} desorption recovery was 82.9% at higher time and intensity using RVM. Dy^{3+} desorption recovery showed a positive correlation with higher intensity and time; recovery increased from 57% to 82.9% as time increased from 5 to 30 min at higher intensity (70%). However, Dy^{3+} desorption recovery increased from 25% to around 40% when the time was increased from 5 min to 30 min at a lower intensity (30%), then decreased after around 23 min.

3.5.2. RVM Multi-Element Desorption

Figure 12a shows the interaction plots of La^{3+} in a multi-element desorption process using 0.5 M nitric acid. The maximum desorption recovery was observed at higher time and intensity using RVM. The desorption recovery showed a positive correlation with time and intensity; La^{3+} desorption increased from 51% to 71.35% as time increased from 5 to 30 min at higher intensity. However, La^{3+} desorption recovery was almost constant with time at lower intensity (30%); it began to decrease around 23 min at 30% intensity. Additional data for all multi-element desorption experiments are provided in the Supplementary Materials.

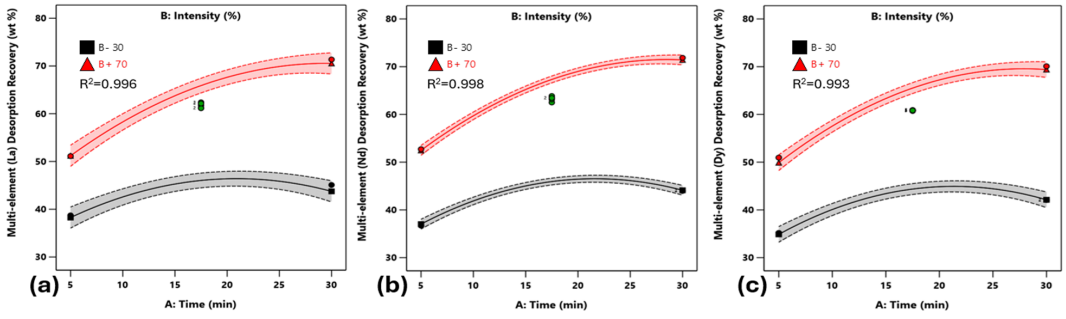

Figure 12. Interaction plots of REE desorption recovery (%) as a function of time (5–30 min) and intensity (30–70%). Model-predicted responses with high confidence intervals (shaded regions). Effect of RVM factors, time, and intensity on REE desorption into the solution from the biochar surface in a multi-element desorption process using 0.5 M nitric acid. (**a**) La^{3+}; (**b**) Nd^{3+}; (**c**) Dy^{3+}.

Figure 12b illustrates the interaction plot of Nd^{3+} desorption recovery in a multi-element desorption process using 0.5 M nitric acid. Similarly, the maximum Nd^{3+} desorption recovery was observed at higher time and intensity using RVM. The Nd^{3+} desorption recovery shows a positive correlation with time and intensity; the Nd^{3+} desorption increased from 52.4% to 71.85% as time increased from 5 to 30 min at 70% intensity. However, Nd^{3+} desorption recovery increased from 5 min to around 22 min at a lower intensity (30%); after that, Nd^{3+} desorption decreased as the time was extended further.

Figure 12c illustrates the interaction plot of Dy^{3+} desorption recovery in a multi-element desorption process using 0.5 M nitric acid. The maximum Dy^{3+} desorption recovery was observed at higher time and intensity using RVM. Dy^{3+} desorption recovery showed a positive correlation with time and intensity; the recovery increased from around 49.8% to 70.08% at higher intensity (70%) as time rose from 5 to 30 min. However, at lower intensity (30%), the Dy^{3+} desorption recovery increased slightly from 35% to around 44% when the time was changed from 5 min to 20 min; after 22 min, the recovery decreased.

REE desorption was performed using 10% oxalic acid (1.11 M) and 0.5 M nitric acid. Figure 13a,b shows a comparison of oxalic and nitric acid REE desorption. The maximum desorption recovery using oxalic acid was reported to be below 10% for La^{3+}, Nd^{3+}, and Dy^{3+} at 30 min, and 70% intensity using RVM. The weak desorption performance of oxalic acid could be due to the lower temperature (below 10 °C) in the RVM machine, where cold water was circulated to keep the reactor cooled. After filtering, precipitation was observed in the scintillation vials. Moreover, oxalic acid is an organic and weak acid compared to nitric acid. It partially dissociates in water. Therefore, to increase the oxalic acid solubility in water, a higher temperature is required. Oxalic acid recovery might increase with increasing temperature. As reported by H.W. Kasaini et al., selective recovery of REE (85–99%) from pregnant leach solutions was achieved using 33% oxalic acid at a temperature range of 85 °C to 95 °C [45].

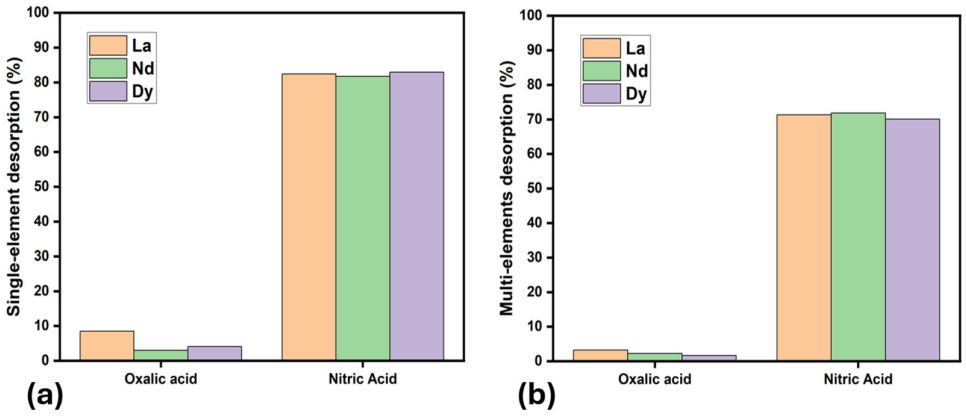

Figure 13. REE desorption recovery (%) comparison of oxalic acid and nitric acid in a single-element (**a**), and multi-element desorption (**b**).

Nitric acid performed better in REE desorption than oxalic acid, proving to be a better desorbent than oxalic acid in single-element and multi-element desorption. The desorption recovery for all REE was primarily affected by intensity and time in both single-element and multi-element desorption because of the higher time and intensity. At higher time and intensity, the collision frequency between the H^+ ions and the hemp biochar surface increased, ion transfer from solution to REE-loaded hemp biochar also increased, and boundary layer resistance was reduced. All these phenomena contributed to higher REE desorption recovery at higher intensity and longer time. The interaction plots of all REE looked identical, showing that nitric acid desorbed all REE almost at the same recovery%, suggesting no desorption selectivity for any REE. The lack of hemp biochar selectivity

might be due to the similar valence states of the REE, as all three are trivalent; they were desorbed at the same rate. Nitric acid protonates the active sites on the biochar, weakening the electrostatic and coordination bonds that hold the REE, allowing them to easily detach from the biochar surface and dissolve in the solution [46,47]. In addition, nitric acid has an acidic pH (0.679 in this study), which lowers the solution pH, thereby dramatically increasing the proton concentration and driving REE desorption via ion exchange [47].

4. Conclusions

With the accelerating demand for REE, it is necessary to develop efficient, eco-friendly extraction techniques. In this work, RVM as a mixing approach and hemp biochar as an adsorbent were assessed for the extraction of REE from synthetic aqueous solutions. The influence of RVM time and intensity, pH conditions, biochar mass, and initial REE concentration was studied.

The hemp biochar efficiently adsorbed REE due to strong electrostatic interactions (pH 5). The maximum adsorption capacities were 77.56 mg/g (Dy^{3+}), 75.85 mg/g (La^{3+}), and 72.65 mg/g (Nd^{3+}), using a Thermo-scientific 4000 M shaker. The adsorption capacity of 100 mg hemp biochar was 79.79 mg/g for Dy^{3+}, followed by 77.61 mg/g for La^{3+} and 75.75 mg/g for Nd^{3+}, using RVM for only 40 min at 70% intensity, indicating RVM as a superior mixing technique. Adsorption reached a plateau at 800 mg/L, indicating saturation of hemp biochar (100 mg). The porosity, large surface area, and negative surface charge on the hemp biochar favored REE adsorption.

REE adsorption exceeded 98% recovery in the single-element system and 83% in the multi-element system for all REE. Both Dy^{3+} and Nd^{3+} exhibited low selectivity under the multi-element conditions. In REE adsorption, the RVM was particularly useful: 30 min at 70% intensity for La^{3+} and Dy^{3+} in the single-element system and for La^{3+}, Nd^{3+}, and Dy^{3+} in the multi-element system. Adsorption of REE onto biochar was attributed to electrostatic attraction, and the Langmuir isotherm model and pseudo-second-order kinetic model well described the adsorption process.

For REE desorption, more than 80% of single-element and 70% of multi-element were obtained with nitric acid by increasing the proton concentration, whereas oxalic acid only partially dissociates and produces fewer protons, which equals lower recovery. Higher RVM intensity favored desorption. In desorption, RVM was effective at 30 min and 70% intensity for all REE in both the single-element and multi-element systems. Hemp biochar and RVM adsorbed REE quickly enough that mixing times as short as 5–30 min can be used at room temperature.

Supplementary Materials: The following supporting information can be downloaded at: https://www.mdpi.com/article/10.3390/met16090959/s1, Table S1: Factorial ANOVA parameters for the Quadratic model and Fit Statistics for La^{3+} adsorption in a single-element adsorption process. Table S2. Factorial ANOVA parameters for the Quadratic model and Fit Statistics for Nd^{3+} adsorption in a single-element adsorption process. Table S3. Factorial ANOVA parameters for the Quadratic model and Fit Statistics for Dy^{3+} adsorption in a single-element adsorption process. Table S4. REE single-element adsorption confirmatory experiments for using RVM. The table presents model-predicted REE recovery (%) and experimental recovery (%) of REE with error %. Table S5. Factorial ANOVA parameters for the Quadratic model and Fit Statistics for La^{3+} adsorption in a multi-element adsorption process. Table S6. Factorial ANOVA parameters for the Quadratic model and Fit Statistics for Nd^{3+} adsorption in a multi-element adsorption process. Table S7. Factorial ANOVA parameters for the Quadratic model and Fit Statistics for Dy^{3+} adsorption in a multi-element adsorption process. Table S8. REE multi-element adsorption confirmatory experiments for using RVM. The table presents model-predicted REE recovery (%) and experimental recovery (%) of REE with error %. Table S9. Factorial ANOVA parameters for the Quadratic model and Fit Statistics for La^{3+} desorption in a

single-element desorption process. Table S10. Factorial ANOVA parameters for the Quadratic model and Fit Statistics for Nd^{3+} desorption in a single-element desorption process. Table S11. Factorial ANOVA parameters for the Quadratic model and Fit Statistics for Dy^{3+} desorption in a single-element desorption process. Table S12. Factorial ANOVA parameters for the Quadratic model and Fit Statistics for La^{3+} desorption in a multi-element desorption process. Table S13. Factorial ANOVA parameters for the Quadratic model and Fit Statistics for Nd^{3+} desorption in a multi-element desorption process. Table S14. Factorial ANOVA parameters for the Quadratic model and Fit Statistics for Dy^{3+} desorption in a multi-element desorption process.

Author Contributions: Conceptualization, M.S. and R.L.; methodology, M.S. and R.L.; software, M.S. and Z.N.; validation, M.S. and R.L.; formal analysis, M.S.; investigation, R.L.; resources, M.S., Z.N. and F.A.; data curation, F.A.; writing—original draft preparation, M.S.; writing—review and editing, M.S., Z.N., F.A. and R.L.; visualization, M.S.; supervision, R.L.; project administration, Z.N.; funding acquisition, R.L. All authors have read and agreed to the published version of the manuscript.

Funding: This research was supported by the Combat Capabilities Development Command Army Research Laboratory (CCDC ARL) through Cooperative Agreement W911NF-22-2-0015, administered by Montana Technological University.

Data Availability Statement: The data presented in this study are openly available in Zenodo at [10.5281/zenodo.20244555], reference number [20244555].

Conflicts of Interest: The authors declare no conflict of interest.

References

1. Chen, Z. Global rare earth resources and scenarios of future rare earth industry. *J. Rare Earths* **2011**, *29*, 1–6. [CrossRef]
2. Abbadi, A.; Mucsi, G. A review on complex utilization of mine tailings: Recovery of rare earth elements and residue valorization. *J. Environ. Chem. Eng.* **2024**, *12*, 113118. [CrossRef]
3. Cheng, S.; Li, W.; Han, Y.; Sun, Y.; Gao, P.; Zhang, X. Recent process developments in beneficiation and metallurgy of rare earths: A review. *J. Rare Earths* **2024**, *42*, 629–642. [CrossRef]
4. dos Reis, G.S.; Srivastava, V.; Taleb, M.F.A.; Ibrahim, M.M.; Dotto, G.L.; Rossatto, D.L.; Oliveira, M.L.S.; Silva, L.F.O.; Lassi, U. Adsorption of rare earth elements on a magnetic geopolymer derived from rice husk: Studies in batch, column, and application in real phosphogypsum leachate sample. *Environ. Sci. Pollut. Res.* **2024**, *31*, 10417–10429. [CrossRef]
5. de O. Salomón, Y.L.; Georgin, J.; dos Reis, G.S.; Lima, É.C.; Oliveira, M.L.S.; Franco, D.S.P.; Netto, M.S.; Allasia, D.; Dotto, G.L. Utilization of Pacara Earpod tree (*Enterolobium contortisilquum*) and Ironwood (*Caesalpinia leiostachya*) seeds as low-cost biosorbents for removal of basic fuchsin. *Environ. Sci. Pollut. Res.* **2020**, *27*, 33307–33320. [CrossRef]
6. Moldoveanu, G.A.; Papangelakis, V.G. Hydrometallurgy Recovery of rare earth elements adsorbed on clay minerals: I. Desorption mechanism. *Hydrometallurgy* **2012**, *117–118*, 71–78. [CrossRef]
7. Singh, R.; Goyal, A.; Sinha, S. Global insights into biochar: Production, sustainable applications, and market dynamics. *Biomass Bioenergy* **2025**, *194*, 107663. [CrossRef]
8. dos Reis, G.S.; Pinto, D.; Lütke, S.F.; Lima, É.C.; Silva, L.F.; De Brum, I.A.; Dotto, G.L. Adsorption of yttrium (Y3+) and concentration of rare earth elements from phosphogypsum using chitin and chitin aerogel. *J. Rare Earths* **2024**, *42*, 775–782. [CrossRef]
9. Agyemang, F.; Saddat, M.; Nasrullah, Z.; LaDouceur, R. Selective Leaching of Rare Earth Elements from Complex Rare Earth Ore Using Deep Eutectic Solvents. In *Metallurgical & Materials Engineering*; Montana Tech: Butte, MT, USA, 2025; Available online: https://digitalcommons.mtech.edu/matr_engr/5 (accessed on 25 January 2026).
10. Zhu, Y.; Zheng, Y.; Wang, A. International Journal of Biological Macromolecules A simple approach to fabricate granular adsorbent for adsorption of rare elements. *Int. J. Biol. Macromol.* **2015**, *72*, 410–420. [CrossRef]
11. Li, J.; Zhu, X.; Zhao, Y.; Yang, M.; Zhang, X.; Chen, H.; Liu, Q. Highly selective recovery of lanthanum and cerium from wastewater by amidoxime-modified biochar. *Sep. Purif. Technol.* **2025**, *371*, 133303. [CrossRef]
12. Jimenez-Lopez, L.; Morales-Ospino, R.; Castro-Gutiérrez, J.; Celzard, A.; Fierro, V. Enhanced hydrogen storage and release capacities when using HKUST-1@activated carbon hybrids obtained by resonant acoustic mixing. *Chem. Eng. J.* **2025**, *520*, 165834. [CrossRef]
13. Riahi, A.; Muretta, J.; Ladouceur, R. Advancing CO_2 separation and capture in post-combustion scenarios using resonant vibration techniques. *Carbon Trends* **2025**, *20*, 100521. [CrossRef]

14. Nasrullah, Z.; Agyemang, F.; Saddat, M.; Ladouceur, R. Process intensification by resonant vibratory mixing for samarium—Cobalt magnet leaching with deep eutectic solvents. *Environ. Sci. Adv.* **2025**, *5*, 510–521. [CrossRef]
15. Nasrullah, Z.; Agyemang, F.; Saddat, M.; Ladouceur, R. Digital Commons @ Montana Tech Process Intensification by Resonant Vibratory Mixing for the Recyclable Samarium—Cobalt Magnets After Chemical Leaching with Deep Eutectic Solvents. In *Metallurgical & Materials Engineering*; Montana Tech: Butte, MT, USA, 2025; Available online: https://digitalcommons.mtech.edu/matr_engr/7/ (accessed on 1 February 2025).
16. Nasrullah, Z. Recovery of High Energy-Value Materials from Mine Wastewater. In *Graduate Theses & Non-Theses*; Montana Tech: Butte, MT, USA, 2025; Available online: https://digitalcommons.mtech.edu/grad_rsch/364 (accessed on 14 April 2026).
17. Shalini, S.S.; Palanivelu, K.; Ramachandran, A.; Raghavan, V. Biochar from biomass waste as a renewable carbon material for climate change mitigation in reducing greenhouse gas emissions—A review. *Biomass Convers. Biorefin.* **2021**, *11*, 2247–2267. [CrossRef]
18. Liu, W.-J.; Jiang, H.; Yu, H.-Q. Development of Biochar-Based Functional Materials: Toward a Sustainable Platform Carbon Material. *Chem. Rev.* **2015**, *115*, 12251–12285. [CrossRef]
19. Shaaban, M.; Abid, M. Chapter 9—Biochar as a sorbent for organic and inorganic pollutants. In *Sorbents Materials for Controlling Environmental Pollution*; Núñez-Delgado, A., Ed.; Elsevier: Amsterdam, The Netherlands, 2021; pp. 189–208. [CrossRef]
20. Famobuwa, V.; Talan, D.; Sanyal, O.; Grushecky, S.; Amini, H. A review of biomass-based adsorption for rare earth elements recovery. *J. Rare Earths* **2025**, *43*, 2311–2321. [CrossRef]
21. Tripathi, M.; Sahu, J.N.; Ganesan, P. Effect of process parameters on production of biochar from biomass waste through pyrolysis: A review. *Renew. Sustain. Energy Rev.* **2016**, *55*, 467–481. [CrossRef]
22. Wang, Y.; Zhao, Y.; He, R.; Yan, Z.; Li, X.; Zhou, H.; Li, N.; Zhi, K.; Song, Y.; Teng, Y.; et al. Effects of Water-Soluble Sodium Compounds on the Microstructure and Combustion Performance of Shengli Lignite. *ACS Omega* **2021**, *6*, 24848–24858. [CrossRef]
23. *ASTM D5373-21*; Test Methods for Determination of Carbon, Hydrogen and Nitrogen in Analysis Samples of Coal and Carbon in Analysis Samples of Coal and Coke. ASTM International: West Conshohocken, PA, USA, 2021. [CrossRef]
24. Al-Harby, N.F.; Albahly, E.F.; Mohamed, N.A. Kinetics, Isotherm and Thermodynamic Studies for Efficient Adsorption of Congo Red Dye from Aqueous Solution onto Novel Cyanoguanidine-Modified Chitosan Adsorbent. *Polymers* **2021**, *13*, 4446. [CrossRef]
25. Anagnostopoulos, V.A.; Symeopoulos, B.D. Sorption of europium by malt spent rootlets, a low cost biosorbent: Effect of pH, kinetics and equilibrium studies. *J. Radioanal. Nucl. Chem.* **2013**, *295*, 7–13. [CrossRef]
26. Kołodyńska, D.; Bąk, J.; Majdańska, M.; Fila, D. Sorption of lanthanide ions on biochar composites. *J. Rare Earths* **2018**, *36*, 1212–1220. [CrossRef]
27. Wang, Y.Y.; Lu, H.H.; Liu, Y.X.; Yang, S.M. Ammonium citrate-modified biochar: An adsorbent for La(III) ions from aqueous solution. *Colloids Surf. A Physicochem. Eng. Asp.* **2016**, *509*, 550–563. [CrossRef]
28. Chen, G.; Viengvilay, K.; Yu, W.; Mao, T.; Qu, Z.; Liang, B.; Chen, Z.; Li, Z. Effect of Different Modification Methods on the Adsorption of Manganese by Biochar from Rice Straw, Coconut Shell, and Bamboo. *ACS Omega* **2023**, *8*, 28467–28474. [CrossRef]
29. Di Virgilio, M.; Latorrata, S.; Cristiani, C.; Dotelli, G. Analysis of the Adsorption-Release Isotherms of Pentaethylenehexamine-Modified Sorbents for Rare Earth Elements (Y, Nd, La). *Polymers* **2022**, *14*, 5063. [CrossRef]
30. Angın, D. Effect of pyrolysis temperature and heating rate on biochar obtained from pyrolysis of safflower seed press cake. *Bioresour. Technol.* **2013**, *128*, 593–597. [CrossRef]
31. Famobuwa, O.V. Characterization and Evaluation of Various Biochar Types as Green Adsorbents for Rare Earth Element Recovery from Aqueous. Master's Thesis, West Virginia University, Morgantown, WV, USA, 2024.
32. Zhang, C.; Ji, Y.; Li, C.; Zhang, Y.; Sun, S.; Xu, Y.; Jiang, L.; Wu, C. The Application of Biochar for CO_2 Capture: Influence of Biochar Preparation and CO_2 Capture Reactors. *Ind. Eng. Chem. Res.* **2023**, *62*, 17168–17181. [CrossRef]
33. Gui, X.; Xu, X.; Zhang, Z.; Hu, L.; Huang, W.; Zhao, L.; Cao, X. Biochar-amended soil can further sorb atmospheric CO_2 for more carbon sequestration. *Commun. Earth Environ.* **2025**, *6*, 5. [CrossRef]
34. Barszcz, W.; Łożyńska, M.; Molenda, J. Impact of pyrolysis process conditions on the structure of biochar obtained from apple waste. *Sci. Rep.* **2024**, *14*, 10501. [CrossRef]
35. Banik, C.; Lawrinenko, M.; Bakshi, S.; Laird, D.A. Impact of Pyrolysis Temperature and Feedstock on Surface Charge and Functional Group Chemistry of Biochars. *J. Environ. Qual.* **2018**, *47*, 452–461. [CrossRef]
36. Sajjadi, B.; Chen, W.-Y.; Egiebor, N.O. A comprehensive review on physical activation of biochar for energy and environmental applications. *Rev. Chem. Eng.* **2019**, *35*, 735–776. [CrossRef]
37. Islam, M.U.; Jiang, F.; Guo, Z.; Peng, X. Does biochar application improve soil aggregation? A meta-analysis. *Soil Tillage Res.* **2021**, *209*, 104926. [CrossRef]
38. Tian, Y.; Chen, Q.; Yan, C.; Deng, H.; He, Y. Classification of Adsorption Isotherm Curves for Shale Based on Pore Structure. *Petrophysics—SPWLA J.* **2020**, *61*, 417–433. [CrossRef]
39. Wu, J.; Wang, N.; Wang, L.; Dong, H.; Zhao, Y.; Jiang, L. Electrospun Porous Structure Fibrous Film with High Oil Adsorption Capacity. *ACS Appl. Mater. Interfaces* **2012**, *4*, 3207–3212. [CrossRef]

40. Liu, L.; Feng, B.; Rao, Y.Z.; Tian, C.S.; Gu, Q.X.; Huang, T. Development of Efficient Biochar Produced from Orange Peel for Effective La(III) and Y(III) Adsorption. *Adsorpt. Sci. Technol.* **2023**, *2023*, 5519783. [CrossRef]
41. Luiz, G.; Pinto, D.; Silva, L.F.O.; Grimm, A.; Khan, M.R.; Ahmad, N.; de Brum, I.A.; Mikkola, J.-P.; dos Reis, G.S. Adsorption of rare earth elements (Ce^{3+}, La^{3+}, and Nd^{3+}) and recovery from phosphogypsum leachate using a novel ZSM-5 zeolite. *Colloids Surf. A Physicochem. Eng. Asp.* **2024**, *698*, 134549. [CrossRef]
42. Anastopoulos, I.; Bhatnagar, A.; Lima, E.C. Adsorption of rare earth metals: A review of recent literature. *J. Mol. Liq.* **2016**, *221*, 954–962. [CrossRef]
43. Kore, A.; Subash, A.; Naebe, M.; Kandasubramanian, B. Application and implementation of chitosan as a potential and sustainable adsorbent for rare earth metal recovery: A review. *Hybrid Adv.* **2024**, *5*, 100175. [CrossRef]
44. Torab-Mostaedi, M.; Asadollahzadeh, M.; Hemmati, A.; Khosravi, A. Biosorption of lanthanum and cerium from aqueous solutions by grapefruit peel: Equilibrium, kinetic and thermodynamic studies. *Res. Chem. Intermed.* **2015**, *41*, 559–573. [CrossRef]
45. Safari, M.; Harris, M.; Deglon, D.; Rondebosch, P.B.; Africa, S. *IMPC 2016: XXVIII International Mineral Processing Congress Proceedings*; Canadian Institute of Mining, Metallurgy and Petroleum: Westmount, QC, Canada, 2016; pp. 1–10.
46. Yan, L.; Gao, G.; Lu, M.; Riaz, M.; Zhang, M.; Tong, K.; Yu, H.; Yang, Y.; Hao, W.; Niu, Y. Insight into the Amelioration Effect of Nitric Acid-Modified Biochar on Saline Soil Physicochemical Properties and Plant Growth. *Plants* **2024**, *13*, 3434. [CrossRef]
47. Rahmati, S.; Adavodi, R.; Romano, P.; Vegliò, F. Evaluation of the mechanisms of rare earth elements extraction from citrate solutions in the recycling of NdFeB magnets. *Process Saf. Environ. Prot.* **2025**, *195*, 106788. [CrossRef]

Disclaimer/Publisher's Note: The statements, opinions and data contained in all publications are solely those of the individual author(s) and contributor(s) and not of MDPI and/or the editor(s). MDPI and/or the editor(s) disclaim responsibility for any injury to people or property resulting from any ideas, methods, instructions or products referred to in the content.